Remote Sensing of Environment 233 (2019) 111365

Contents lists available at ScienceDirect

Remote Sensing of Environment

journal homepage: www.elsevier.com/locate/rse

Sea surface salinity subfootprint variability estimates from regional high-resolution model simulations

Joseph M. D'Addezio[a,*], Frederick M. Bingham[b], Gregg A. Jacobs[a]

[a] Naval Research Laboratory, Ocean Dynamics and Prediction, MS, USA
[b] University of North Carolina at Wilmington, Department of Physics and Physical Oceanography, NC, USA

ARTICLE INFO

Edited by Menghua Wang

Keywords:
Sea surface salinity
Subfootprint variability
Modeling

ABSTRACT

Sea surface salinity (SSS) subfootprint variability (SFV) is estimated using high-resolution, realistically forced regional simulations of the Arabian Sea and western Pacific with an integration period of one year. A weighted standard deviation was calculated for footprint sizes of 100 km, 40 km, 20 km, and 10 km for all model time steps and then median (σ_{50}) and 95th percentile (σ_{95}) values were calculated along the time dimension. An additional method, wavenumber spectral analysis (σ_k), was also employed to obtain a different but comparable estimate. σ_{50} and σ_{95} maxima (>1 psu) are found in shallow waters along the continental shelves where strong river outflow is present. Open ocean values of both statistics are much lower ($\sim$0.1 psu). The wavenumber spectral analysis allowed the estimation of total SSS spatial variance over 640 km, which was then compared to the estimates obtained by integrating time-averaged SSS power spectral density (PSD) at wavelengths $\leq$100 km, 40 km, 20 km, and 10 km. For both geographic regions, the ratio of variance at and below each wavelength to the total variance across all estimated wavelengths is approximately 50%, 30%, 15%, and 5%, respectively. σ_{50}, σ_{95}, and σ_k magnitudes as a function of footprint size follow a power-law relationship. The observed strong decline in SSS SFV below 40 km suggests that the current effective resolution of the SMAP and SMOS satellites is advantageous for limiting the impact of SFV on the satellites' error budget.

1. Introduction

Beginning this decade, three unique remote sensing platforms, Soil Moisture Ocean Salinity (SMOS; Mecklenburg et al., 2012), Aquarius SAC-D (Lagerloef, 2012), and Soil Moisture Active Passive (SMAP; Fore et al., 2016), have greatly enhanced understanding of global sea surface salinity (SSS) distribution and variability. An important and ongoing element within each mission is to reduce retrieval errors below the current standard: 0.2 psu STDE (standard deviation of the error) on monthly time scales and spatial scales of 100 km × 100 km (Hasson et al., 2013; Drucker and Riser, 2014; Hernandez et al., 2014). Validation, and therefore performance assessment, of the remotely sensed SSS measurements remains challenging in part because of ocean salinity characteristics that remain poorly understood. Firstly, the sensor makes a passive measurement of the ocean surface that senses only the first couple of centimeters or less of the water column (Lagerloef et al., 2008). The majority of in situ measurements used for validation purposes, such as those collected by Argo floats, are taken several meters below the ocean surface. On a number of temporal and spatial scales, vertical salinity stratification induced by surface forcing and oceanic processes can cause discrepancies between the measurement retrieved by the satellite and the in situ observation made below the surface (Henocq et al., 2010; Drucker and Riser, 2014; Boutin et al., 2016). Secondly, no observing system can perfectly sample all ocean phenomena at all of their respective frequencies. Longer sampling periods introduce greater opportunity for high-frequency events to become aliased into the lower-frequency signals the instrument can confidently observe. With respect to the SSS sensing satellites, this problem has been quantified to some extent (Vinogradova and Ponte, 2012), but remains an active area of research interest. The final significant source of difference between in situ point measurements and the satellite observation is due to subfootprint variability (SFV) (Vinogradova and Ponte, 2013; Boutin et al., 2016). The engineering characteristics of each satellite (i.e. the size of the antenna and wavelength detected by the radiometer) dictate that measurements are averages within a circular or elliptic area known as the “footprint”. The footprint is approximately 100 km for Aquarius and 40 km for SMOS & SMAP (Lagerloef, 2012; Kerr et al., 2010; Fore et al., 2016). An in situ measurement taken within the footprint can differ substantially from that estimated by the satellite depending on the magnitude of the spatial

* Corresponding author at: Naval Research Laboratory, Ocean Dynamics and Prediction, 1009 Balch Blvd., Stennis Space Center, MS 39529, USA.
E-mail address: joseph.daddezio@nrlssc.navy.mil (J.M. D'Addezio).

https://doi.org/10.1016/j.rse.2019.111365
Received 30 November 2018; Received in revised form 1 August 2019; Accepted 7 August 2019
0034-4257/ Published by Elsevier Inc.

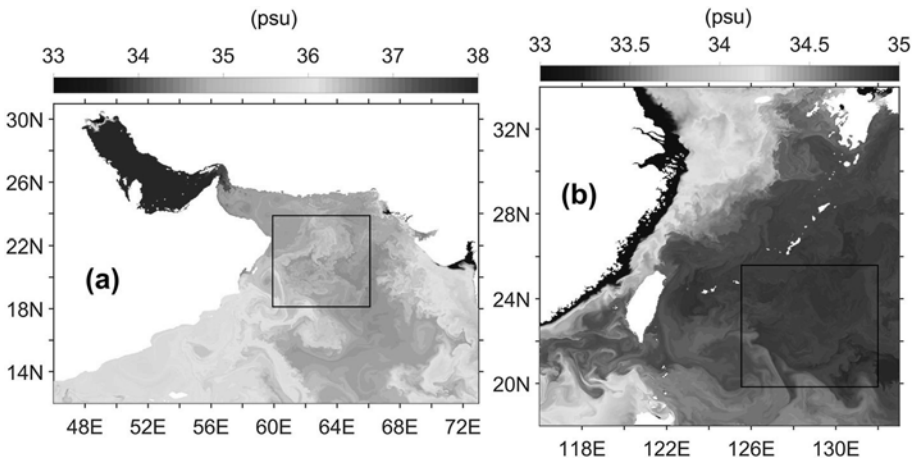

Fig. 1. Snapshot of Navy Coastal Ocean Model (NCOM) sea surface salinity (SSS; psu) in the (a) Arabian Sea (46°E-73°E; 12°N-31°N) and (b) western Pacific (116°E-133°E; 18°N-34°N). The black boxes in the Arabian Sea (60°E-66°E; 18°N-24°N) and western Pacific (126°E-132°E; 20°N-26°N) denote the sub-regions over which wavenumber spectral analyses were performed.

variance of SSS within the footprint. This phenomenon has not been sufficiently quantified leaving uncertainty about how accurate the satellite SSS measurements really are. If the satellite SSS data are to be properly validated, some estimate of this representation error must be obtained and factored into the satellite error budgets. With this information, better satellite calibration can be performed leading to a more accurate SSS product. Here, we aid this effort by providing novel estimates of SSS SFV using a high-resolution (1 km) ocean general circulation model (OGCM) in two regions of the global ocean that each feature different spatiotemporal SSS variability.

A wide spectrum of physical phenomena on differing time and spatial scales could be responsible for the presence of significant SFV. Western boundary currents are characterized by strong fronts with spatial scales on the order of the current generation of SSS remote sensing platforms' footprints. Mesoscale eddies are responsible for the majority of horizontal surface stirring that can cause large SSS variance on length scales between approximately 200–50 km (Capet et al., 2008). The mesoscale horizontal length scales are dictated by the Rossby radius of deformation that is a function of latitude and vertical stratification (Chelton et al., 1998). Below the local deformation radius, submesoscale eddies, fronts, and filaments could be responsible for strong SSS variability, although this phenomenon is much less well understood than its mesoscale equivalent (McWilliams, 2016). High-frequency rainfall events can substantially alter SSS on spatial scales that range from global to atmospheric submesoscales (Boutin et al., 2016). Strong river outflow in regions such as the Gulf of Mexico, mouth of the Amazon river, and the Bay of Bengal cause strong gradients in SSS that have been regularly observed by the SSS satellites (Grodsky et al., 2012; Gierach et al., 2013; Reul et al., 2014; Fournier et al., 2015; Korosov et al., 2015). Finally, in polar regions, ice melt/formation can produce substantial SSS gradients (Brucker et al., 2014).

Observing this continuum of ocean physics using in situ observations can be challenging. Stationary buoy networks must trade high-density measurements in space and time for large-scale geographic coverage or vice versa. Ocean cruises can collect data over large areas at high spatial and temporal resolutions, but specific locations are sampled infrequently in time. Field campaigns that can achieve high spatiotemporal coverage over regional scales (e.g. SPURS-1 and SPURS-2; Lindstrom et al., 2015; SPURS-2 Planning Group, 2015), are highly effective but rare and have only been implemented over a very small percentage of the global ocean for relatively short stretches of time. In contrast, OGCMs provide complete geographic coverage at high spatial and temporal resolutions. This comes at the expense of instantaneous accuracy, but a long ensemble of model forecasts can produce a physically realistic body of statistics (e.g. Kelly et al., 2007). Therefore, OGCMs that explicitly resolve the continuum of ocean physics described above can provide useful estimates of SSS SFV on regional and global scales.

This approach has been previously taken by Vinogradova and Ponte (2013) to derive Aquarius-like estimates of the SSS SFV phenomenon using an iteration of the assimilative global HYbrid Coordinate Ocean Model (HYCOM). They found large SSS SFV values exceeding 1 psu in coastal outflow regions such as the Amazon and Mississippi rivers. Western boundary currents and high latitude regions also featured strong SSS SFV of the order of 0.2 psu and greater. Open ocean estimates generally fell below 0.2 psu. The methods used in this experiment are an extension of that previous work, whereby we use an OGCM that explicitly resolves a wider range of ocean physics and we estimate SSS SFV over a larger set of footprints.

The material is arranged by first detailing the numerical model and the data analysis procedure used to create the SSS SFV estimates in Section 2. Two methods are employed: a derivation of the weighted standard deviation within several footprint sizes and wavenumber spectral analysis. Section 3 details the results produced by both methods and ultimately a comparison of the SSS SFV magnitudes produced by each. Section 4 summarizes the results, notes the potential utility of the information gathered, and highlights possible directions for producing more robust results in future experiments.

2. Methods

2.1. Modeling

Two regions within the global ocean are analyzed in this study: the Arabian Sea (46°E–73°E; 12°N–31°N) and the western Pacific (116°E–133°E; 18°N–34°N). Each region features unique ocean dynamics that make them interesting for analysis. The Arabian Sea (Fig. 1a) has strong seasonal salinity, temperature, dynamic height, and velocity transitions associated with the semi-annual monsoon (Schott and McCreary Jr, 2001). Although predominantly an evaporative semi-enclosed basin, strong precipitation associated with the southwest monsoon, advection of freshwater from the Bay of Bengal during the northeast monsoon, and strong regional river outflow can all generate substantial salinity gradients along the continental shelf and within the open ocean. Salt-water outflow also occurs at the mouth of the Persian Gulf. In the western Pacific (Fig. 1b), the Kuroshio dominates the variability of the region, meanders of which can create strong temperature, dynamic height, and velocity gradients. The region features a broad continental shelf with substantial river outflow along most of it. Lacking strong seasonal forcing like that present in the Arabian Sea, the western Pacific open ocean salinity variability is primarily controlled by localized, high-frequency precipitation events (e.g. tropical storms) and ocean mesoscale and submesoscale dynamics.

Simulated ocean fields of each region were generated using the

Navy Coastal Ocean Model (NCOM) (Barron et al., 2006). NCOM is a primitive equation model that uses the Boussinesq and hydrostatic approximations to numerically solve for scalar and vector ocean fields on a regular three-dimensional grid. The vertical coordinate is a hybrid σ/z grid, useful for greater terrain following capabilities in the coastal ocean and enhanced representation of the near surface dynamics in the open ocean. In this experiment, 50 vertical layers were used, with the σ/z transition occurring at approximately 120 m. The horizontal grid was set to 1 km, allowing the simulation to explicitly resolve ocean phenomena with submesoscale spatial scales (~10 km) (Capet et al., 2008). Boundary conditions, ultimately derived from a 1/12° global HYCOM simulation, were introduced into the final 1 km NCOM grid using a two-nest framework. Boundary conditions were generated from global HYCOM and passed into a 3 km NCOM simulation at least 3° larger than the final 1 km NCOM grid on all sides. Boundary conditions from the 3 km NCOM simulation were then generated and passed into the final 1 km NCOM grids for both the Arabian Sea and western Pacific. This was done to avoid numerical instabilities that can occur when interpolating boundary conditions from a global model at least three times coarser than the final, higher resolution regional grid. Solar radiation, surface wind stress, latent and sensible heat flux, and precipitation were generated using output from the NAvy Global Environmental Model (NAVGEM; Hogan et al., 2014). Freshwater input from large river mouths were introduced into the simulation using the NCOM river database (Barron and Smedstad, 2002). Barotropic tides were applied to the ocean interior and to velocities at the open boundaries using the Oregon Tidal Inverse Solution (OTIS) (Egbert and Erofeeva, 2002). This combination of oceanic, atmospheric, and tidal modeling constitutes a highly realistic system.

The simulation was initialized on December 1, 2015 and then spun up for a duration of one month to allow the proper development of synoptic, mesoscale, and submesoscale dynamics. Forward integration continued through December 31, 2016, generating a complete annual dataset with 3 hourly output available for data analysis. Observations of the real ocean were not assimilated. While data assimilation is useful for generating short- to medium-term skill in ocean prediction (Cummings et al., 2009), this is not the purpose of the modeling framework used in this study. Instead, we are collecting an ensemble of estimates of SSS spatial variance from model fields that include a comprehensive set of physics. However, if the long term statistics of the model solution deviated too far from the climatological statistics of the real ocean, results derived from such a system may not be applicable to the real ocean. The statistics of the simulation are evaluated against a climatology of the real ocean to ensure that the results detailed in Section 3 are a reasonable approximation of real ocean SSS SFV.

The Generalized Digital Environmental Model version 4 (GDEM4) (Teague et al., 1990; Carnes et al., 2010) is an observation based climatology that is used here for comparison with the long-term statistics produced by NCOM. The GDEM4 climatology was compiled using in situ observations from delayed-mode Argo, the Navy's Master Oceanographic Observation Data Set (MOODS), and the World Ocean Database (WOD) 2005. The data were binned onto a $^1/_4° \times {}^1/_4°$ grid and means and standard deviations were derived. This coarse spatial resolution will mask variance due to small-scale features that may be present in the model simulations. To confirm, we performed weighted footprint means of the model SSS and took the variance across time (not shown). The variances of the smoothed models fields tend to compare more favorably with the GDEM4 variances, suggesting that differences in data set resolution are a potentially large source of mismatch. Additionally, the vast majority of the surface salinity observations come from Argo floats (Carnes et al., 2010; see their Fig. 2). The Argo floats are designed to profile the top 1000 m of the water column every 10 days. This makes it difficult for the observing network to represent coastal phenomena as well as transient features in the open ocean. Finally, independent of the limitations of the climatology, the NCOM simulations are not perfect representations of the physics found in the real ocean. The simulations are still coarse enough to exclude important physical processes (e.g. Langmuir circulation), use imperfect numerical schemes, and make physical assumptions in the form of parameterizations. These will all lead to mismatch between the model variability and the real ocean variance. Noting the potential issues associated with each dataset, our goal is to confirm that the SSS variability in the NCOM simulations at least qualitatively compares favorably with the variability observed in the GDEM4 climatology. The results of that comparison are presented below.

Fig. 2 shows annual SSS standard deviation from the 1 km NCOM solution and climatological SSS standard deviation from GDEM4 for the Arabian Sea. To the southwest and in the interior of the domain, relatively low values of SSS standard deviation (~0.2 psu) are prevalent in both data sets. To the southeast of the domain, larger values are observed (~0.6 psu), and are associated with seasonal surface and subsurface salinity variability caused by the monsoon transition in the Arabian Sea mini warm pool (Rao and Sivakumar, 2003; Nyadjro et al., 2012). NCOM features much stronger SSS standard deviation along the northeastern expanse of the region than the GDEM4 climatology. As previously mentioned, the climatology is coarse and based on in situ observations that do not properly sample the coastal dynamics that NCOM can simulate due to the inclusion of river runoff from the NCOM river database. Finally, strong SSS standard deviation (> 1 psu) is present in the Persian Gulf in both datasets. In all, the two datasets compare favorably with respect to the magnitude and spatial distribution of annual SSS standard deviation in the Arabian Sea. The same analysis was repeated for the western Pacific (Fig. 3). In this region, the highest SSS standard deviation (> 2 psu) is confined to the broad continental shelf where river outflow is strong. The open ocean presents the greatest difference between the two datasets. Both include lower magnitude SSS standard deviation (~0.2 psu), but NCOM has consistently lower magnitudes than GDEM4. This suggests that open ocean SSS SFV estimates described in Section 3 may underestimate those found in the real ocean in the western Pacific.

To summarize, SSS annual standard deviations compare well between the two datasets in both of the regions under investigation here. The primary difference was found in the coastal regions where the GDEM4 climatology is not able to resolve strong river outflow. In the western Pacific, open ocean SSS standard deviations were consistently lower than that found in the GDEM4 climatology. The next section describes the two methodologies used to derive regional estimates of SSS SFV: weighted subfootprint standard deviations and wavenumber spectral analysis.

2.2. Data analysis

The first method used to estimate SSS SFV from our model fields most closely replicates the way that the SSS sensing satellites calculate subfootprint means. Each model grid (Arabian Sea and western Pacific) was partitioned into subgrids with spacing d_o = [100 km; 40 km; 20 km; 10 km], where d_o is the footprint radius. At each grid point of the new subgrid, a weighted sample standard deviation was calculated over a circle with diameter $2d_o$:

$$\sigma = \sqrt{\frac{\sum w_i (S_i - \overline{S})^2}{\sum w_i}} \tag{1}$$

$$w_i = e^{-\ln(2)\left(\frac{d_i}{0.5 d_o}\right)^2} \tag{2}$$

where S_i is model SSS value at a grid point with location i within the footprint, $\overline{S}$ is the sample mean of all values within the footprint, and d_i is the physical distance from the central grid point to grid point i within the footprint. This formulation most closely mimics the antenna pattern of the real aperture radiometers used by Aquarius and SMAP (T. Meissner and F. Wentz, personal communication). Eq. (2) shows weights that produce an exponential decay with value 1 at the central

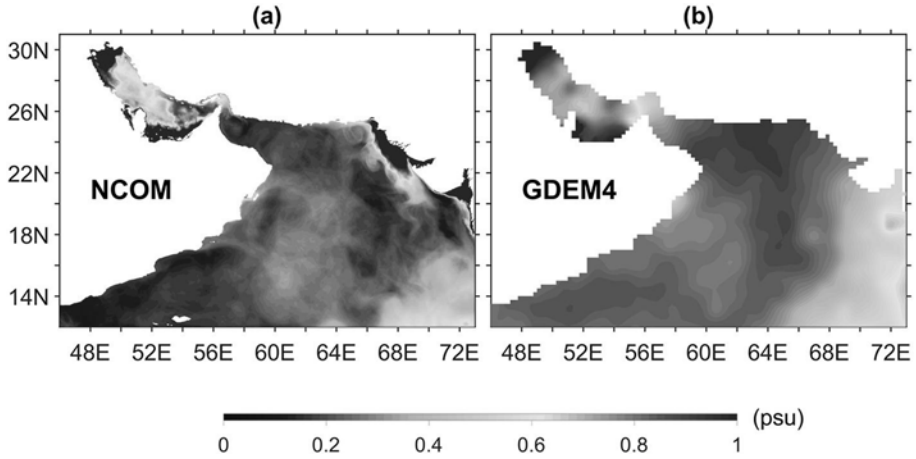

Fig. 2. Annual sea surface salinity (SSS) standard deviation (psu) in the Arabian Sea from the (a) Navy Coastal Ocean Model (NCOM) and (b) the GDEM4 climatology.

grid point, 0.5 at distance $0.5d_o$ from the central grid point, and 0.063 at distance d_o from the central grid point (Fig. 4). This specific configuration of the weighted footprint may not be as applicable to the types of measurements the SMOS synthetic aperture radar makes.

Each of the subgrids begins length d_o from the boundaries of each of the model domains. This was done to ensure that each iteration of Eq. (1) had a complete set of data, instead of having to introduce new assumptions at the boundaries to account for the lack of data outside the model domains. Weighted SSS standard deviations were calculated for each subgrid at each model time step ($N = 2928$). From the resulting time-space matrix, median and 95th percentile values were calculated along the time dimension (Boutin et al., 2016). Hereafter, these statistics are called σ_{50} and σ_{95}, respectively. σ_{50} provides an estimate of some typical value of SSS SFV, while σ_{95} provides an estimate of an outlier instance.

Wavenumber spectral analysis provides a convenient methodology to decompose the model SSS variance as a function of spatial scale. Model SSS power spectral density (PSD) was calculated over subregions of both the Arabian Sea and western Pacific (Fig. 1) for all 2928 model time steps. The ensemble of PSD in k_x, k_y wavenumber space was then averaged to generate a time mean estimate. A common way of visualizing how the PSD changes as a function of wavelength is to produce a one-dimensional spectrum. This was achieved using the time mean PSD and azimuthally averaging along constant wavenumbers to compute $\overline{PSD}(k)$ (i.e. averaged along concentric circles from the smallest wavenumbers to the largest) (e.g. Richman et al., 2012; Wong and Skamarock, 2016; Durran et al., 2017; and references therein) (Fig. 5). Both the Arabian Sea and western Pacific spectra produce an unbroken cascade of $\overline{PSD}(k)$ from the largest of observed scales down to our Nyquist wavelength. The spectra of the two domains have similar slopes; each calculated using a power-law relationship in log-log coordinates:

$$y = b * x^m \tag{3}$$

where b is the y-intercept and m is the slope. The slopes for both regions compare favorably with the k^{-3} power-law frequently associated with kinetic energy (KE) spectra in Earth's atmosphere and ocean (e.g. Khatri et al., 2018; and references therein). Ocean salinity often acts as a passive tracer, being advected and stirred in both the horizontal and vertical by the synoptic, mesoscale, and submesoscale currents. For this reason, it is unsurprising that the spectral slopes are comparable to those derived for velocity. However, both regions feature slopes that are slightly steeper than the velocity power-law. At the surface, salinity variability is also strongly influenced by atmospheric forcing (evaporation minus precipitation; E-P). Spatial variability associated with evaporation is very large-scale, while precipitation can have both large-scale (e.g. intertropical convergence zone; ITCZ) and small-scale (e.g. isolated convection) contributions (Yu, 2011). Both surface forcing effects could be making the spectral slopes both steeper and flatter. By taking a long-term average of the PSD, it becomes difficult, if not

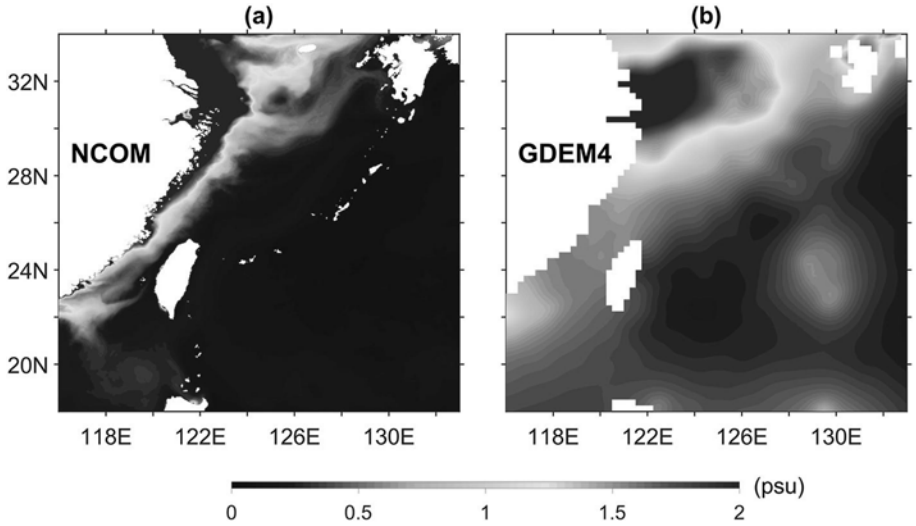

Fig. 3. Same as Fig. 2, but for the western Pacific.

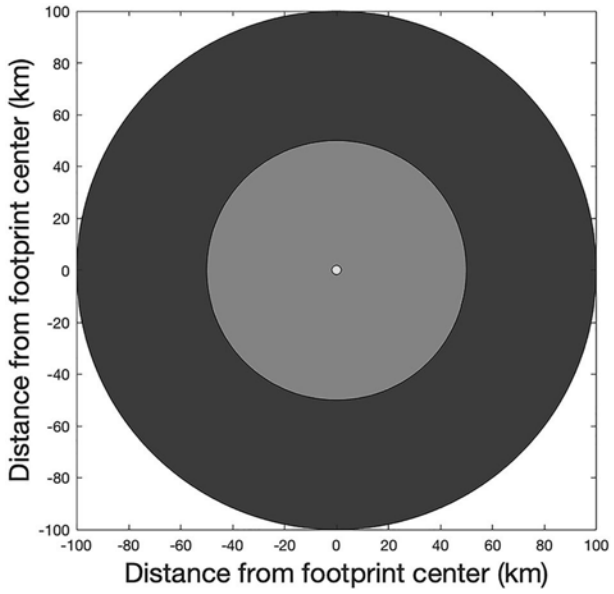

Fig. 4. Schematic view of the weighting within the footprint for a footprint size of 100 km. The estimate is made at the central point indicated in yellow. Grid points within the light blue area have weights, $0.5 \leq w_i \leq 1$. Grid points in the dark blue area have weights, $0.063 \leq w_i < 0.5$. Grid points outside the blue areas are not used to estimate the value at the central point in the model, though those areas would have some small influence on an actual satellite measurement. (For interpretation of the references to color in this figure legend, the reader is referred to the web version of this article.)

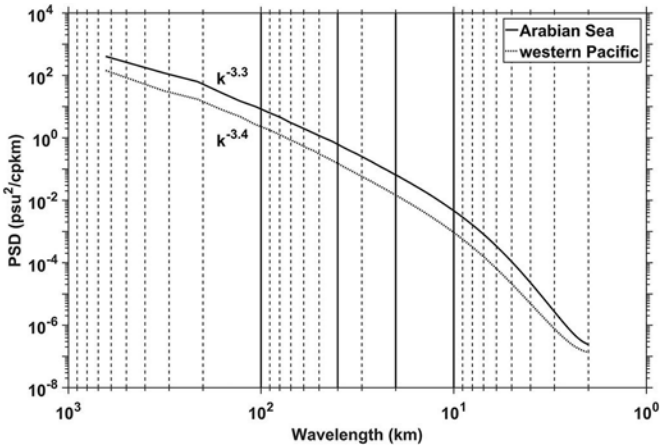

Fig. 5. Space-time averaged sea surface salinity (SSS) wavenumber spectra (psu^2/cpkm) for subregions of the Arabian Sea (black line) and western Pacific (dashed black line). See Fig. 1 for geographic reference to the subregions used to calculate the spectra. The indicated spectral slopes were derived over the 100 km–10 km wavelength range using the power-law relationship shown in Eq. (3). Vertical solid black lines denote the wavelengths integrated over in Eq. (4) to get estimates of SSS subfootprint variability (SFV).

impossible, to tease apart the specific contributions from the oceanic turbulence and the atmospheric forcing. Thus, our analysis of the spatial variance using wavenumber spectra includes the entanglement of all of these effects, as would be the case for an instantaneous, satellite-derived snapshot of SSS.

Averaging, however, does not recover variance from the two-dimensional PSD. According to Parseval's theorem, integration of the time mean PSD provides the SSS variance:

$$\sigma_k = \sqrt{\int_k^{k_n} \int_{-\pi}^{\pi} \overline{PSD}(k) k d\theta dk} \quad (4)$$

where $k = \sqrt{k_x^2 + k_y^2}$ are the wavenumber bands azimuthally integrated along and under ($1/100\,km^{-1}$, $1/40\,km^{-1}$, $1/20\,km^{-1}$, and $1/10\,km^{-1}$) and k_n is the Nyquist wavenumber ($1/2\,km^{-1}$). Eq. (4) provides the SSS spatial variance at and below a defined length scale and is therefore a different but analogous estimate of SSS SFV to that produced using Eqs. (1) and (2). Note that Eq. (4) has limitations. The method will not account for the disparate zonal and meridional correlation scales of SSS (Bingham and Lee, 2017; see their Fig. 7). Additionally, the spectral method does not include coastlines and islands, restricting our spectral analysis to open ocean regions. Despite these potential issues, we will show the method to be a powerful tool, precisely because it provides more nuanced information about SSS spatial variance than possible when using only the weighted subfootprint standard deviations (Eqs. (1) and (2)).

Magnitudes and spatial distributions of σ_{50}, σ_{95}, and σ_k in the Arabian Sea and western Pacific are presented in Sections 3.1 and 3.2. In Section 3.3, the three SSS SFV estimates are compared to understand the differences in each methodology and how each statistic changes as a function of footprint size.

3. Results

3.1. SSS subfootprint variance

σ_{50} within the Arabian Sea shows a wide range of geographically dependent magnitudes (Fig. 6). For all four footprint sizes (100 km, 40 km, 20 km, and 10 km), the largest magnitudes are found within the Persian Gulf and along the continental shelf at the mouth of large rivers. Across the footprint sizes, magnitudes are much lower within the open ocean. Examining differences in magnitudes between the footprint sizes, the 100 km footprint generates the highest levels of SSS SFV for all subregions of the Arabian Sea (Fig. 6a). In the Persian Gulf and along the continental shelf, σ_{50} estimates exceed 1 psu. In the open ocean, σ_{50} is highest for the 100 km footprint as well. This suggests significant horizontal heterogeneity in SSS variability that is likely a function of both large-scale atmospheric forcing and oceanic mesoscale stirring. Using the 40 km footprint (Fig. 6b), we observe a very similar geographic distribution of σ_{50} maxima and minima, but overall magnitudes are lower across the domain. This is most significant in the open ocean, as the 40 km σ_{50} magnitudes drop by up to 0.1 psu compared to the 100 km σ_{50} estimates. σ_{50} from the 20 km (Fig. 6c) and 10 km (Fig. 6d) footprints repeat this decrease in magnitude between the 100 km and 40 km footprints, but with a smaller reduction in σ_{50} magnitude in the open ocean. By the 10 km footprint, almost all of the open ocean variability has disappeared with σ_{50} at or below 0.05 psu.

In the same region using the same footprint sizes, σ_{95} was also estimated (Fig. 7). For the 100 km footprint (Fig. 7a), the σ_{95} values follow almost exactly the same geographic pattern of maxima and minima as the σ_{50} estimate, but with much higher overall magnitudes. This is to be expected as the σ_{95} value is demonstrating the set of extreme SSS SFV events across the time series. Very high σ_{95} values (> 2 psu) are found in the Persian Gulf and at the mouth of major rivers, but open ocean magnitudes now also exceed 0.3 psu over much of the domain. Within the 40 km footprint (Fig. 7b), σ_{95} values in the open ocean fall back below 0.3 psu with the exception to the Arabian Sea mini warm pool region in the southeastern Arabian Sea. This trend continues moving to the 20 km footprint (Fig. 7c), but interesting geographic patterns in σ_{95} emerge within the 10 km footprint (Fig. 7d). In the open ocean, intersecting lines of σ_{95} are observed with magnitudes around 0.15 psu. These features are physical and represent strong SSS fronts that are present along the model time series. This suggests the presence of strong mesoscale and submesoscale fronts that can infrequently produce relatively high instantaneous SSS SFV in the open ocean, even when using a relatively small footprint.

σ_{50} in the western Pacific (Fig. 8) has many of the same spatial

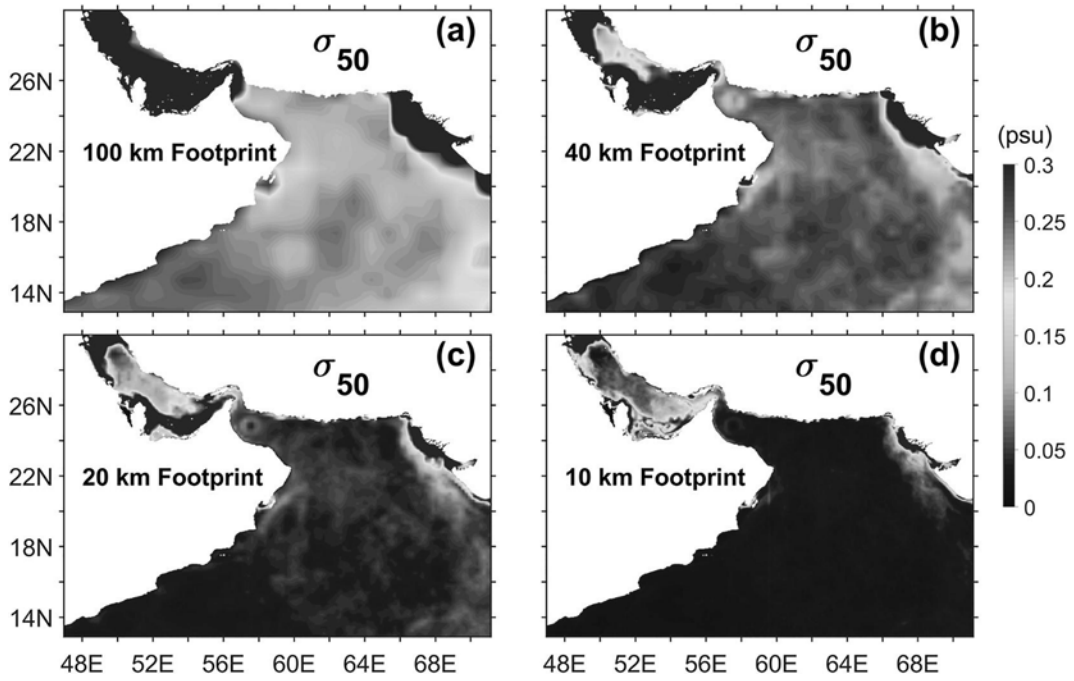

Fig. 6. Arabian Sea σ_{50} (psu) for footprint sizes (a) 100 km, (b) 40 km, (c) 20 km, and (d) 10 km.

patterns as that observed in the Arabian Sea. Along the continental shelf, σ_{50} is higher magnitude due to strong river outflow from the western landmass. Off the shelf, open ocean σ_{50} magnitudes are greatly diminished, similar to the Arabian Sea. Overall, open-ocean magnitudes are lower than those observed in the Arabian Sea. With respect to specific footprints, the 100 km footprint (Fig. 8a) has the highest magnitudes in the open ocean (0.1 psu) and the greatest eastward extension of high σ_{50} maxima (> 1 psu) along the continental shelf. A steady decline in open ocean σ_{50} magnitudes are observed moving down from the 100 km footprint to the 40 km footprint (Fig. 8b) to the 20 km footprint (Fig. 8c) and finally to the 10 km footprint (Fig. 8d). A gradual decrease of the eastward extension in the σ_{50} maxima along the shelf is also observed along the same decrease in footprint size.

Finally, σ_{95} in the western Pacific (Fig. 9) is detailed. Across the model domain, σ_{95} magnitudes are much greater than those produced by σ_{50} in both the open ocean and along the continental shelf, although the geographic distribution of maxima and minima are consistent. For the 100 km footprint (Fig. 9a), σ_{95} values exceed 2 psu along the shelf and are around 0.15 psu in the open ocean. A coarse outline of the Kuroshio western boundary current is evident inshore of the Ryukyu island chain. The 40 km footprint (Fig. 9b) shows an overall reduction in σ_{95} magnitude, less eastward extent of the shelf maxima, and a clearer representation of the western boundary current. At 20 km (Fig. 9c), the pattern of magnitude reduction continues. We observe

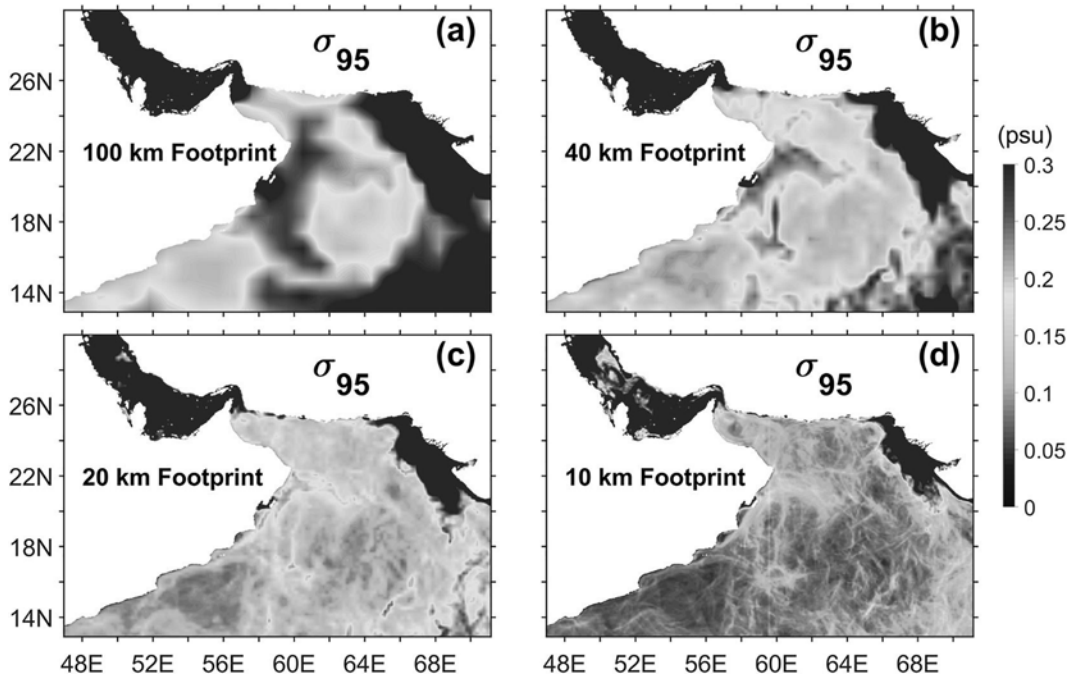

Fig. 7. Same as Fig. 6, but for σ_{95} (psu).

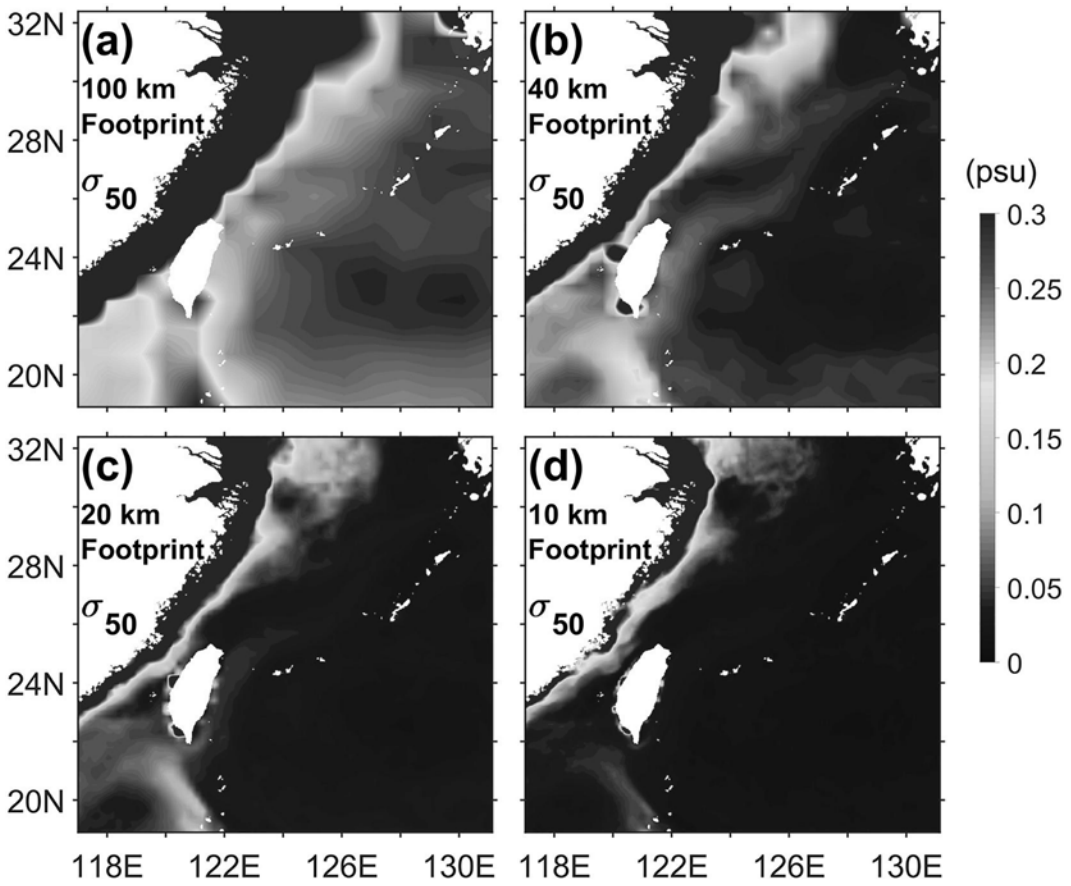

Fig. 8. Western Pacific σ_{50} (psu) for footprint sizes (a) 100 km, (b) 40 km, (c) 20 km, and (d) 10 km.

additional refinement of the visual representation of the Kuroshio, although its σ_{95} maximum is reduced. The bright, intersecting lines observed in the Arabian Sea (Fig. 7d) are also observable with magnitudes of approximately 0.1 psu. Finally, the 10 km footprint (Fig. 9d) demonstrates a very defined western boundary current with reduced magnitude as well as a much clearer expression of the frontal features observed in the western Pacific 20 km footprint (Fig. 9c) and the Arabian Sea 10 km footprint (Fig. 7d). The clear presence of the Kuroshio front in the 20 km and 10 km σ_{95} results further suggests that the smaller lines observed in the open ocean of both model domains are strong fronts that occurred infrequently during the full 2016 model integration period.

Calculating weighted standard deviations within a series of footprint sizes allowed the observation of several consistent results. The largest magnitude σ_{50} and σ_{95} values were found along the shelf where strong river outflow is present, or in the case of the Persian Gulf, strong salinity fronts exist in the shallow, evaporative semi-enclosed basin. The open ocean featured much lower magnitude SSS SFV and limited spatial variability in the 100 km and 40 km footprints. At 20 km and 10 km, however, the presence of strong fronts generated higher magnitude spatial variability in σ_{95} for both model domains. The next section also provides model derived SSS SFV results, but instead through the use of wavenumber spectral analysis.

3.2. SSS wavenumber spectrum

Integrating across the time mean, two-dimensional PSD, according to Eq. (4), provides an estimate of SSS integrated variance at and below a particular wavelength. This is comparable to the weighted subfootprint standard deviations shown in Section 3.1, because that method also estimates the total variance at and below a particular length scale. For direct comparison with the weighted subfootprint standard deviations, the 100 km, 40 km, 20 km, and 10 km wavelengths were chosen to integrate at and below. These wavenumber spectra derived SSS SFV estimates are shown in Fig. 10. For the Arabian Sea (Fig. 10a), we obtain a quantitative estimate of the decline in SSS SFV as a function of length scale that we observed qualitatively in Section 3.1. Comparison with the total integrated standard deviation shows that the 100 km wavelength has 52% of the total standard deviation at and below it, 29% for 40 km, 16% for 20 km, and 7% for 10 km. In the western Pacific (Fig. 10b), we obtain different magnitudes, but similar ratios: 48%, 25%, 14%, and 6%, respectively. It would be tempting to hypothesize the potential universality of open ocean SSS SFV ratios, but the true situation is likely more complicated. The spectral slopes of the SSS PSD in both regions have very similar magnitudes (Fig. 5), leading to similar ratios. Global sea surface height wavenumber spectra vary substantially geographically (Xu and Fu, 2010), suggesting that the geostrophically balanced mesoscale dynamics that strongly influence horizontal SSS variability vary in similar ways. Analysis of a high-resolution global model would help to elucidate the possibility of geographically independent ratios of open-ocean SSS SFV.

The results presented above are region-specific. The results can be generalized using the wavenumber spectral analysis, given a known PSD power-law slope and y-intercept. Please see Appendix A for the derivation of this generalized solution for σ_k. The results are presented in Fig. 11, with region-specific SSS PSD slopes at our chosen footprint sizes overlain for reference. As expected, σ_k decreases with decreasing footprint size for any given spectral slope. Although we have only analyzed two regions of the global ocean, the results demonstrated in Fig. 11 (and derived in Appendix A) can be used to estimate σ_k for any region given a known local PSD slope and y-intercept. It is also variable independent, so while we present results using slopes and y-intercepts

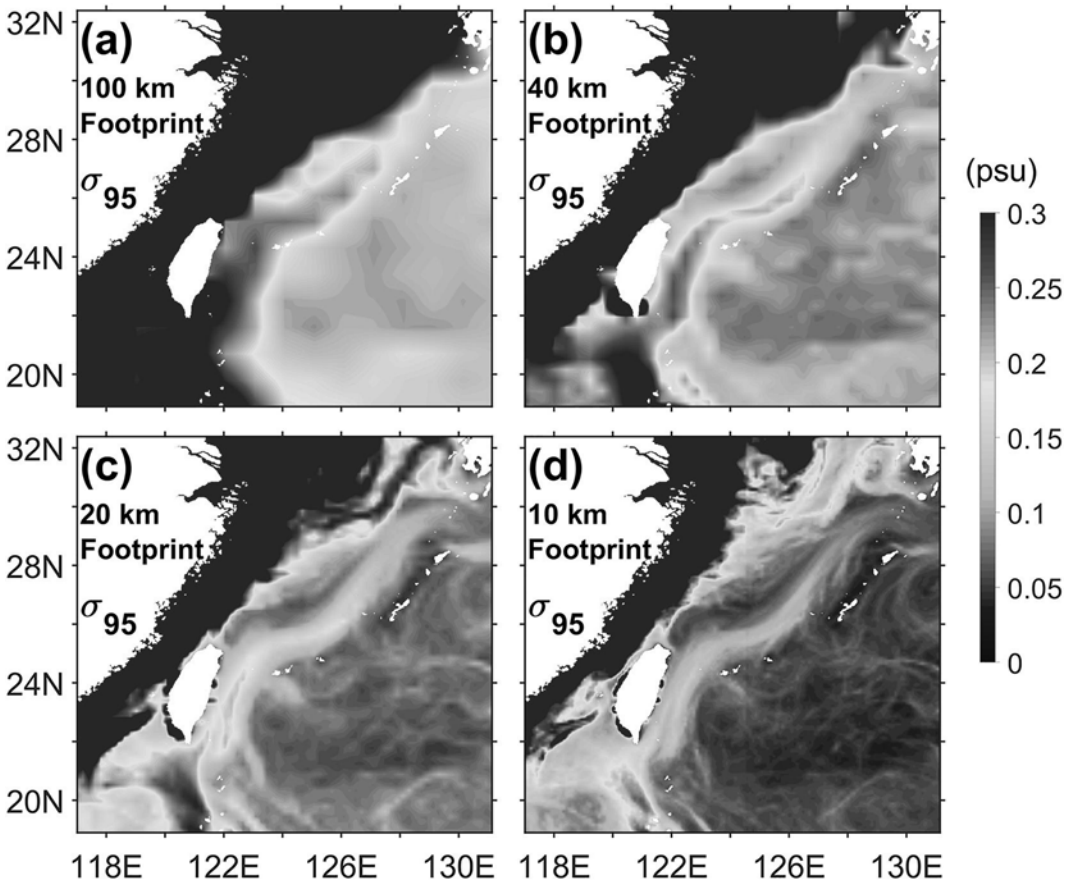

Fig. 9. Same as Fig. 8, but for σ_{95} (psu).

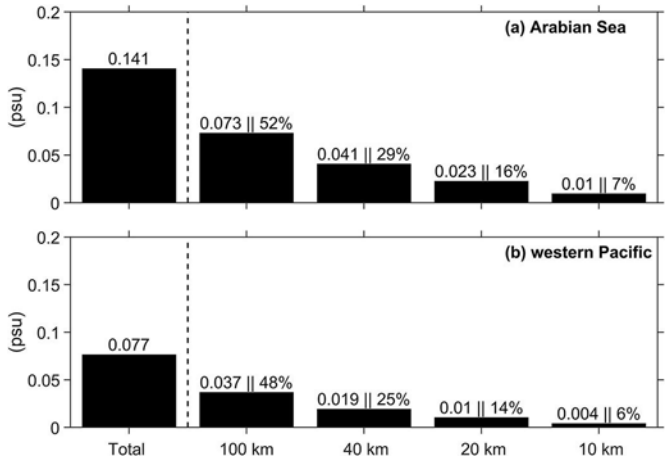

Fig. 10. Estimates of sea surface salinity (SSS) subfootprint variability (SFV) (psu) derived through integration of temporally averaged power spectral density (PSD) per Eq. (4) (σ_k) from subregions of the (a) Arabian Sea and (b) western Pacific. The total value represents the integration of PSD over all observed wavelengths (640 km–2 km). The specified wavelengths represent the magnitude of SSS SFV by integrating at and below that wavelength (e.g. 100 km–2 km). Percentages are the ratio of the SSS SFV magnitude derived for each wavelength and the total value.

specific to Arabian Sea and western Pacific SSS, the method could be applied to any geophysical parameter with PSD that follows a power-law relationship (e.g. sea surface temperature).

From the perspective of current and future sampling techniques, these results are encouraging. They suggest that even when using a relatively coarse footprint (e.g. the 100 km footprint of Aquarius), approximately 50% of the total synoptic variance is muted by the footprint average. The finer 40 km footprint, typical of SMOS and SMAP, limits approximately 70% of the variance. Moving towards smaller footprints produces diminishing returns as a 20 km (10 km) footprint limits approximately 85% (95%) of the total variance. This does not suggest that enhancing the resolution of the satellite is a useless venture; a higher resolution product will allow the observation of important physics (e.g. small mesoscales, submesoscales, storm-scale freshwater puddles, etc.). The results suggest instead that increasing the resolution beyond 40 km does not dramatically change the impact of SSS SFV on the satellite error budget to the same extent that moving from 100 km to 40 km does. In Section 3.3, we compare the results derived by the two different methodologies presented in Sections 3.1 and 3.2 to better understand the relationship between SSS SFV and footprint size.

3.3. Comparison of SSS SFV estimates

σ_{50} and σ_{95} were averaged over the same geographic domains over which wavenumber spectral analyses were performed (Fig. 1) and compared with the results derived in Section 3.2. These results are presented in Table 1. In both domains and for all footprint sizes, σ_{95} produces the highest magnitudes followed by σ_{50} and then σ_k. In Table 1, although the decrease in magnitude with decreasing footprint size is evident, it is not immediately obvious if the pattern is linear. To the contrary, Fig. 11 suggests that σ_k has a nonlinear decline with decreasing footprint size. To better visualize the phenomenon, Fig. 12 provides a graphical representation of Table 1 in a log-log coordinate. The optimal fit to each of the lines is a power-law relationship (Eq. (3)). With respect to σ_k, this is not a necessarily surprising result. The SSS PSD follows a power-law relationship between 100 km–10 km, and it

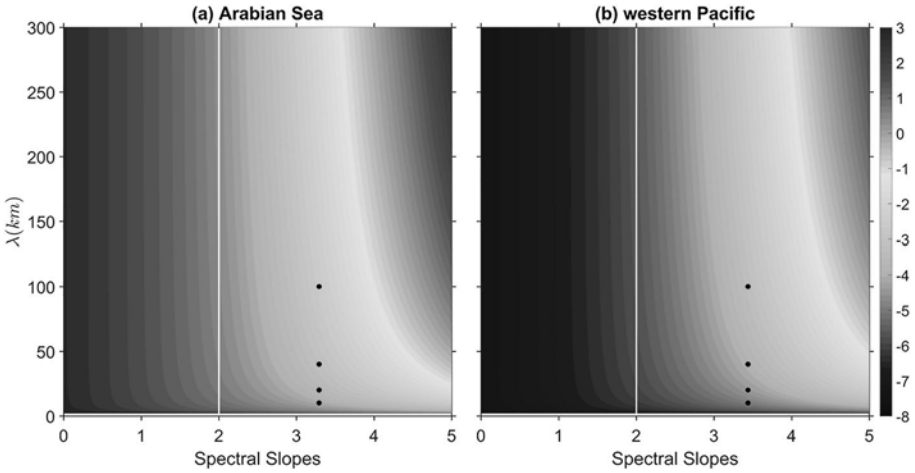

Fig. 11. log(σ_k) (color) as a function of variable spectral slopes and wavelengths in the (a) Arabian Sea and (b) western Pacific. The black dots in each subplot show σ_k at the 100 km, 40 km, 20 km, and 10 km wavelengths and each region's sea surface salinity (SSS) spectral slope per Fig. 5: 3.3 and 3.4 for the Arabian Sea and western Pacific, respectively. Differences in magnitude between (a) and (b) are due to the use of region specific y-intercepts in each calculation.

Table 1
Arabian Sea and western Pacific sea surface salinity (SSS) subfootprint variability (SFV) (psu) estimates from the three different statistics examined. $\overline{\sigma_{95}}$ and $\overline{\sigma_{50}}$ are spatial means of σ_{95} and σ_{50} over the subregions of the Arabian Sea and western Pacific shown in Fig. 1.

	Arabian Sea			Western Pacific		
	$\overline{\sigma_{95}}$	$\overline{\sigma_{50}}$	σ_k	$\overline{\sigma_{95}}$	$\overline{\sigma_{50}}$	σ_k
100 km	0.22	0.11	0.07	0.12	0.05	0.04
40 km	0.17	0.07	0.04	0.1	0.03	0.02
20 km	0.14	0.05	0.02	0.07	0.02	0.01
10 km	0.1	0.03	0.01	0.05	0.01	0.004

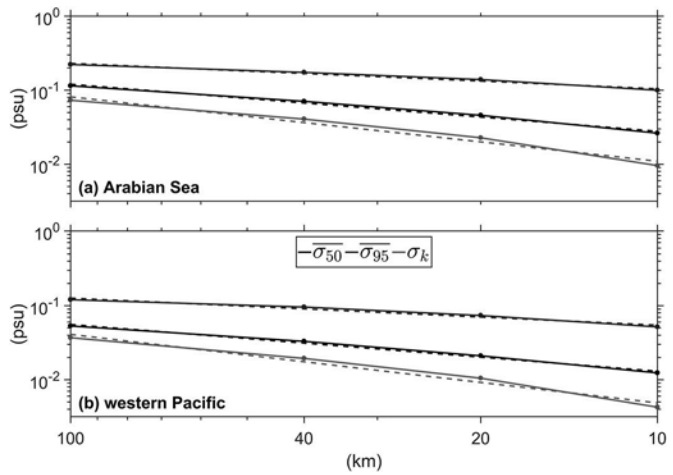

Fig. 12. Sea surface salinity (SSS) subfootprint variability (SFV) (psu) derived from each methodology ($\overline{\sigma_{95}}$, $\overline{\sigma_{50}}$, and σ_k) for all the examined footprint sizes in the (a) Arabian Sea and (b) western Pacific. Line colors and methods are matched at the top of the bottom panel. $\overline{\sigma_{95}}$ and $\overline{\sigma_{50}}$ are spatial means of σ_{50} and σ_{95} over the same subdomains shown in Fig. 1 within which wavenumber spectral analyses were performed. These data are also listed in Table 1. Dashed lines of the corresponding color are power-law fits (Eq. (3)) to each set of data.

can be shown that this dictates that the slope of σ_k must also follow a power-law relationship with a derivable theoretical magnitude (see Appendix A). Slopes of the least squares power-law fit to each line in Fig. 12 are shown in Table 2. The Arabian Sea and western Pacific observed and theoretical slopes of σ_k are comparable, though values are appreciably different. This is likely due to the fact that the power-law slope derived for PSD (Fig. 5) does not hold all the way to the Nyquist wavelength. Coincidentally, the σ_{50} slopes in both regions also compare

Table 2
Slopes from least squares power-law fits to the data shown in Table 1 and Fig. 12. Theoretical wavenumber derived slopes are listed in the bottom-most column. Please see Appendix A for how the theoretical values were determined.

	Arabian sea			Western Pacific		
	$\overline{\sigma_{95}}$	$\overline{\sigma_{50}}$	σ_k	$\overline{\sigma_{95}}$	$\overline{\sigma_{50}}$	σ_k
Observed slope	0.34	0.63	0.87	0.36	0.63	0.93
Theoretical slope	N/A	N/A	0.65	N/A	N/A	0.7

well with the theoretical slopes of σ_k. The Arabian Sea and western Pacific σ_{95} slopes are flatter than both the σ_{50} and σ_k values. Because all three statistics, in both regions are well fit by a power-law relationship, this suggests that the SSS SFV phenomenon as a function of footprint size has a power-law scaling.

This finding is consistent with the observations made in Sections 3.1 and 3.2, wherein we noted diminished returns in reducing SSS SFV beyond the 40 km footprint. The nonlinear relationship between SSS SFV and footprint size observed here is also of note. It would be useful to check the validity of this result using both observations and other regional & global high-resolution simulations to see if it can be reproduced in multiple open ocean scenarios. Fig. 11 suggests that the phenomenon may be universal. With more robust validation, this power-law relationship could be used to reduce the influence of SFV on in situ – satellite mismatch in validation efforts.

4. Summary and conclusions

Model-derived estimates of SSS SFV have been generated in the Arabian Sea and western Pacific using two different methodologies: weighted subfootprint SSS standard deviation and wavenumber spectral analysis. From the first method, two terms were derived: σ_{50} and σ_{95}. Both featured regional maxima (> 1 psu) along the continental shelf near river mouths and shallow, evaporative semi-enclosed basins. Open ocean values of both were much lower than in the coastal regions, with magnitudes around 0.1 psu. σ_{95} featured interesting line formations within footprint sizes of 20 km and 10 km. This phenomenon was associated with strong SSS fronts that occurred infrequently during the 2016 model integration period.

Wavenumber spectral analysis produced similar results, but provided additional information. Using a 100 km footprint, approximately 50% of the synoptic SSS spatial variance is contained at scales larger than the footprint. This ratio was approximately 70%, 85%, and 95% for the 40 km, 20 km, and 10 km footprints, respectively. This suggests a substantial decrease in SSS SFV between 100 km and 40 km, but diminishing returns below this value. This is encouraging, as both the

SMOS and SMAP satellite use footprint sizes of approximately 40 km. This is not to suggest that nothing can be gained by increasing the effective resolution of remotely sensed salinity products. New physical processes will be observed by a higher-resolution system. Our results merely suggest that SSS SFV becomes a much smaller source of in situ - satellite mismatch below the 40 km footprint. This conclusion is ultimately driven by the observation of a nonlinear decrease in SSS SFV with decreasing footprint size. Our results were best fit by a power-law relationship no matter which methodology or statistic was used (Fig. 12).

This preliminary work shows strong promise for correcting remotely sensed SSS observations with respect to SSS SFV induced mismatch. A geographically dependent estimate of SSS SFV with a power-law decay in magnitude could be built to approximate instantaneous SSS SFV within a particular footprint. This important step cannot be taken confidently without first expanding upon the analysis shown here. Both our model domains are within the subtropics, precluding any analysis of SSS SFV due to ice melt/formation in the polar regions. These effects could be substantial and should be investigated further. We plan to extend this work to a high-resolution global system to develop more geographically complete estimates. An additional consideration should also be that the median and 95th percentile SSS SFV show large gaps in magnitude (i.e. high SSS SFV variance), as the phenomenon was not explored thoroughly here. Finally, these model-based solutions should be sanity checked against the best available observation-based estimates to reach consensus on this important subject. With all of this additional information, the satellite community should then have the requisite knowledge to include a more sophisticated estimation of representation error produced by SFV in the salinity satellites' error budget. However, in the intermediary, the results demonstrated in Fig. 11 could be used as a method for estimating SSS SFV for any given footprint size, assuming the universality of a power-law distribution of SSS PSD and by having some estimate of SSS PSD spectral slopes and y-intercepts on a global grid.

Acknowledgements

This research is funded by the Naval Research Laboratory base program Submesoscale Prediction of Eddies by Altimeter Retrieval (SPEAR). FMB was supported by NASA under grant #80NSSC18K1322. The authors are thankful for two anonymous reviewers and the editor who provided constructive comments that improved the manuscript.

Appendix A

We desire a theoretical framework to determine the slope of the sea surface salinity (SSS) spatial variance as a function of wavenumbers integrated along and under ($k \rightarrow k_{Nyquist}$). We observe a power-law scaling of the azimuthally averaged power spectral density (PSD) (Fig. 5)

$$y(k) = b * k^{-m} \tag{A.1}$$

where b is the y-intercept, $k = \sqrt{k_x^2 + k_y^2}$, and m is the PSD slope when viewed as a log-log plot. We now insert Eq. (A.1) into Eq. (4):

$$\sigma_k = \sqrt{\int_k^{k_n} \int_{-\pi}^{\pi} bk^{-m} k d\theta dk} \tag{A.2}$$

where k_n is the Nyquist wavenumber. Integrated first with respect to θ, Eq. (A.2) yields:

$$\sigma_k = \sqrt{\int 2\pi b k^{1-m} dk} \tag{A.3}$$

Evaluating the indefinite integral with respect to k yields:

$$\sigma_k = \sqrt{\left(\frac{2\pi b}{2-m}\right) k^{2-m} + C} \tag{A.4}$$

$$\sigma_k = \sqrt{Bk^{2-m} + C} \tag{A.5}$$

where B now contains both the y-intercept and the multiplicative byproducts of the indefinite integration. We further assume that $C = 0$, a reasonable assumption as $\sigma_k \rightarrow 0$ when $k \rightarrow k_n$, which yields:

$$\sigma_k = \sqrt{B} k^{1-\frac{m}{2}} \tag{A.6}$$

Converting from wavenumber to wavelength $\left(\lambda = \frac{1}{k}\right)$, we can now solve for a theoretical slope of σ_k assuming some constant, power-law slope of the PSD ($m = 3.3$ for the Arabian Sea in Fig. 5):

$$\sigma_k = \sqrt{B} \lambda^{\frac{m}{2}-1} = \sqrt{B} \lambda^{\frac{3.3}{2}-1} = \sqrt{B} \lambda^{0.65} \tag{A.7}$$

Table 2 shows how the theoretical values derived using Eq. (A.7) compare with the slopes derived from the least squares power-law fit to the data shown in Table 1 and Fig. 12.

Additionally, if we evaluate Eq. (A.3) as a definite integral we obtain:

$$\sigma_k = \sqrt{\frac{2\pi b}{m-2}(k^{2-m} - k_n^{2-m})} \tag{A.8}$$

Converting from wavenumber to wavelength yields:

$$\sigma_k = \sqrt{\frac{2\pi b}{m-2}(\lambda^{m-2} - \lambda_n^{m-2})} \tag{A.9}$$

Results obtained using the region specific y-intercepts are shown in Fig. 11. Note that Eqs. (A.8) and (A.9) provide a generalized method for obtaining SFV estimates for any footprint size and any geophysical variable (e.g. sea surface temperature), assuming that the PSD of the variable follows a power-law distribution.

References

Barron, C.N., Smedstad, L.F., 2002. Global river inflow within the Navy Coastal Ocean model. In: Proceedings MTS/IEEE Oceans 2002 Conference, pp. 781–786.

Barron, C.N., Kara, A.B., Martin, P.J., Rhodes, R.C., Smedstad, L.F., 2006. Formulation, implementation and examination of vertical coordinates choices in the Global Navy Coastal Ocean Model (NCOM). Ocean Model. 11, 347–375. https://doi.org/10.1016/j.ocemod.2005.01.004.

Bingham, F., Lee, T., 2017. Space and time scales of sea surface salinity and freshwater forcing variability in the global ocean (60°S–60°N). J. Geophys. Res. Oceans 122, 2909–2922. https://doi.org/10.1002/2016JC012216.

Boutin, J., Chao, Y., Asher, W.E., Delcroix, T., Drucker, R., Drushka, K., Kolodziejczyk, N., Lee, T., Reul, N., Reverdin, G., Schanze, J., Soloviev, A., Yu, L., Anderson, J., Brucker, L., Dinnat, E., Santos-Garcia, A., Jones, W.L., Maes, C., Meissner, T., Tang, W., Vinogradova, N., Ward, B., 2016. Satellite and in situ salinity: understanding near-surface stratification and subfootprint variability. Bull. Am. Meteorol. Soc. 1391–1407. https://doi.org/10.1175/BAMS-D-15-00032.1.

Brucker, L., Dinnat, E.P., Koenig, L.S., 2014. Weekly gridded Aquarius L-band radiometer/scatterometer observations and salinity retrievals over the polar regions – part 2: initial product analysis. Cryosphere 8, 915–930. https://doi.org/10.5194/tc-8-915-2014.

Capet, X., McWilliams, J.C., Molemaker, M.J., Shchepetkin, A.F., 2008. Mesoscale to submesoscale transition in the California current system part I: flow structure, eddy flux, and observational tests. J. Phys. Oceanogr. 38, 29–43. https://doi.org/10.1175/2007JPO3671.1.

Carnes, M., Helber, R.W., Barron, C.N., Dastugue, J.M., 2010. Validation test report for GDEM4. In: NRL Tech Report NRL/MR/7330–10-9271, (Available from NRL, code 7330, Bldg. 1009, Stennis Space Center, MS 39529-5004).

Chelton, D.B., DeSzoeke, R.A., Schlax, G., Naggar, K.E., Siwertz, N., 1998. Geographical variability of the first baroclinic Rossby radius of deformation. J. Phys. Oceanogr. 28, 433–460.

Cummings, J., Bertino, L., Brasseur, P., Fukumori, I., Kamachi, M., Martin, M.J., Mogensen, K., Oke, P., Testut, C.E., Verron, J., Weaver, A., 2009. Ocean data assimilation systems for GODAE. Oceanography 22 (3), 96–109. https://doi.org/10.5670/oceanog.2009.69.

Drucker, R., Riser, S.C., 2014. Validation of Aquarius sea surface salinity with Argo: analysis error due to depth of measurement and vertical salinity stratification. J. Geophys. Res. Oceans 119, 4626–4637. https://doi.org/10.1002/2014JC010045.

Durran, D., Weyn, J.A., Menchaca, M.Q., 2017. Practical considerations for computing dimensional spectra from gridded data. Mon. Wea. Rev. 145, 3901–3910. https://doi.org/10.1175/MWR-D-17-0056.1.

Egbert, G.D., Erofeeva, S.Y., 2002. Efficient inverse modeling of barotropic ocean tides. J. Atmos. Ocean. Technol. 19, 183–204.

Fore, A., Yueh, S., Tang, W., Stiles, B., Hayashi, A., 2016. Combined active/passive retrievals of ocean vector wind and sea surface salinity with SMAP. IEEE Trans. Geosci. Remote Sens. 54, 7396–7404. https://doi.org/10.1109/TGRS.2016.2601486.

Fournier, S., Chapron, B., Salisbury, J., Vandemark, D., Reul, N., 2015. Comparison of spaceborne measurements of sea surface salinity and colored detrital matter in the Amazon plume. J. Geophys. Res. Oceans 120, 3177–3192. https://doi.org/10.1002/2014JC010109.

Gierach, M.M., Vazquez-Cuervo, J., Lee, T., Tsontos, V.M., 2013. Aquarius and SMOS detect effects of an extreme Mississippi River flooding event in the Gulf of Mexico. Geophys. Res. Lett. 40, 5188–5193. https://doi.org/10.1002/grl.50995.

Grodsky, S.A., et al., 2012. Haline hurricane wake in the Amazon/Orinoco plume: AQUARIUS/SACD and SMOS observations. Geophys. Res. Lett. 39, L20603. https://doi.org/10.1029/2012GL053335.

Hasson, A., Delcroix, T., Boutin, J., 2013. Formation and variability of the South Pacific Sea surface salinity maximum in recent decades. J. Geophys. Res. Oceans 118, 5109–5116. https://doi.org/10.1002/jgrc.20367.

Henocq, C., Boutin, J., Petitcolin, F., Reverdin, G., Arnault, S., Lattes, P., 2010. Vertical variability of near-surface salinity in the tropics: consequences for L-band radiometer calibration and validation. J. Atmos. Ocean. Technol. 27, 192–209. https://doi.org/10.1175/2009JTECHO670.1.

Hernandez, O., Boutin, J., Kolodziejczyk, N., Reverdin, G., Martin, N., Gaillard, F., Reul, N., Vergely, J.L., 2014. SMOS salinity in the subtropical North Atlantic salinity maximum: 1. Comparison with Aquarius and in situ salinity. J. Geophys. Res. Oceans 119, 8878–8896. https://doi.org/10.1002/2013JC009610.

Hogan, T.F., et al., 2014. The navy global environmental model. Oceanography 27, 116–125. https://doi.org/10.5670/oceanog.2014.73.

Kelly, K.A., Thompson, L., Cheng, W., Metzger, E.J., 2007. Evaluation of HYCOM in the Kuroshio extension region using new metrics. J. Geophys. Res. Oceans 112, C01004. https://doi.org/10.1029/2006JC003614.

Kerr, Y.H., et al., 2010. The SMOS mission: new tool for monitoring key elements of the global water cycle. Proc. IEEE 98, 666–687. https://doi.org/10.1109/JPROC.2010.2043032.

Khatri, H., Sukhatme, J., Kumar, A., Verma, M.K., 2018. Surface ocean enstrophy, kinetic energy fluxes, and spectra from satellite altimetry. J. Geophys. Res. Oceans 123, 3875–3892. https://doi.org/10.1029/2017JC013516.

Korosov, A., Counillon, F., Johannessen, J.A., 2015. Monitoring the spreading of the Amazon freshwater plume by MODIS, SMOS, Aquarius, and TOPAZ. J. Geophys. Res. Oceans 120, 268–283. https://doi.org/10.1002/2014JC010155.

Lagerloef, G., 2012. Satellite mission monitors ocean surface salinity. EOS, Trans. Amer. Geophys. Union 93, 233–234. https://doi.org/10.1029/2012EOS250001.

Lindstrom, E., Bryan, F., Schmitt, R., 2015. SPURS: salinity processes in the upper-ocean regional study – the North Atlantic experiment. Oceanography 28 (1), 14–19. https://doi.org/10.5670/oceanog.2015.01.

McWilliams, J.C., 2016. Submesoscale currents in the ocean. Proc. R. Soc. A. 472, 20160117. https://doi.org/10.1089/rspa.2016.0117.

Mecklenburg, S., et al., 2012. ESA's soil moisture and ocean salinity Mission: Mission performance and operations. IEEE Trans. Geosci. Remote Sens. 50, 1354–1366. https://doi.org/10.1109/TGRS.2012.21877666.

Nyadjro, E.S., Subrahmanyam, B., Murty, V.S.N., Shriver, J.F., 2012. The role of salinity on the dynamics of the Arabian Sea mini warm pool. J. Geophys. Res. Oceans 117, C09002. https://doi.org/10.1029/2012JC007978.

Rao, R.R., Sivakumar, R., 2003. Seasonal variability of sea surface salinity and salt budget of the mixed layer of the North Indian Ocean. J. Geophys. Res. 108 (C1), 3009. https://doi.org/10.1029/2001JC000907.

Reul, N., Quilfen, Y., Chapron, B., Fournier, S., Kudryaztsev, V., Sabia, R., 2014. Multisensor observations of the Amazon-Orinoco river plume interactions with hurricanes. J. Geophys. Res. Oceans 119, 8271–8295. https://doi.org/10.1002/2014JC010107.

Richman, J.G., Arbic, B.K., Shriver, J.F., Metzger, E.J., Wallcraft, A.J., 2012. Inferring dynamics from the wavenumber spectra of an eddying global ocean model with embedded tides. J. Geophys. Res. 117, C12012. https://doi.org/10.1029/2012JC008364.

Schott, F.A., McCreary Jr., J.P., 2001. The monsoon circulation of the Indian Ocean. Prog. Oceanogr. 51, 1–123. https://doi.org/10.1016/S0079-6611(01)00083-0.

SPURS-2 Planning Group, 2015. From salty to fresh – salinity processes in the upper-ocean regional Study-2 (SPURS-2): diagnosing the physics of a rainfall-dominated salinity minimum. Oceanography 28 (1), 150–159. https://doi.org/10.5670/oceanog.2015.15.

Teague, W.J., Carron, M.J., Hogan, P.J., 1990. A comparison between the generalized digital environment model and Levitus climatologies. J. Geophys. Res. 95 (C5), 7167–7183.

Vinogradova, N.T., Ponte, R.M., 2012. Assessing temporal aliasing in satellite-based surface salinity measurements. J. Atmos. Ocean. Technol. 29 (9), 1391–1400. https://doi.org/10.1175/JTECH-D-11-00055.1.

Vinogradova, N.T., Ponte, R.M., 2013. Small-scale variability in sea surface salinity and implications for satellite-derived measurements. J. Atmos. Ocean. Technol. 30 (11), 2689–2694. https://doi.org/10.1175/JTECH-D-13-00110.1.

Wong, M., Skamarock, W.C., 2016. Spectral characteristics of convective-scale precipitation observations and forecasts. Mon. Wea. Rev. 114, 4183–4196. https://doi.org/10.1175/MWR-D-16-0183.1.

Xu, Y., Fu, L.-L., 2010. Global variability of the wavenumber spectrum of oceanic mesoscale turbulence. J. Phys. Oceanogr. 41, 802–809. https://doi.org/10.1075/2010JPO4558.1.

Yu, L., 2011. A global relationship between the ocean water cycle and near-surface salinity. J. Geophys. Res. Oceans 116, C10025. https://doi.org/10.1029/2010JC006937.